Chapter 7

Optical Devices Based on Symmetrical Metal Cladding Waveguides

Lin Chen

Additional information is available at the end of the chapter

http://dx.doi.org/10.5772/48146

1. Introduction

Controlling and guiding light with planar waveguide has a great potential to fabricate attractive optical devices such as modulators [1], filters [2] and sensors [3]. Although many studies use planar waveguide made of dielectric materials or semiconductors, metals also play an important role in this field. Metals have been usually used as mirror in the visible or infrared regions. By constructing the dielectric layer sandwiched by two metal layers and forming the metal-dielectric-metal (MDM) structure, we can obtain the unique optical properties which the dielectric planar waveguides do not have. Recently, Shin *et al*. reported that this structure can function as the negative refraction lens for surface plasmon waves on a metal surface. This structure provides a new way of controlling the propagation of surface plasmons, which are important for nanoscale manipulation of optical waves [4].

This type of MDM can be expected to have the interesting optical features not only in the negative refraction index but also in the mode properties. The above mentioned waveguide structure can commonly accommodate only surface plasmon mode. When the thickness of guiding layer is increased to millimeter-scale, such waveguide can accommodate thousands of guided modes, and ultrahigh-order modes (UHM) can be excited. In this case the MDM is commonly called symmetrical metal-cladding waveguide (SMCW) [5]. To our knowledge, however, there have been few investigations about the UHM properties of the SMCW. In this chapter, we have reported the UHM properties of the SMCW and their applications on optical devices. The UHM of SMCW can be excited by free space coupling [6] in small incident angle. In section 2, we present some details of the UHM properties such as large mode spacing, sensitive to the change of waveguide parameters, and slow wave effect. Section 3 introduces applications on optical devices such as modulators, filters and sensors, which are closely related to the UHM in guiding layer.

2. Properties of SMCW

The SMCWs are the millimeter-scale guiding layers (dielectric constant ε_1, thickness d) sandwiched between two metal films (Fig.1). The upper metal film (dielectric constant ε_2, thickness h) of several dozens of nanometer acts as coupling layer as well as a metal cladding; and the base metal layer (dielectric constant ε_2) acts as a substrate of the waveguide, which is thick enough to prevent the influence of the glass flat on guiding layer. For modulation applications, the upper and base metal films also serve as electrodes of the device. If the light incidents from air to the guiding layer directly, it can meet the coupling condition and couple the mode with effective index less than 1. The allowed range of the effective index in SMCW can be reached from 0 to n_1 for the guided modes, where $n_1 = (\varepsilon_1)^{1/2}$ is the refractive index of the guiding slab. This range is much wider than that available to the usual waveguides. The principle model of free-space coupling is shown in Fig.2. When the beam incomes from the air to the metal surface, it will generate evanescent field in the metal. Since the upper metal film is thin (dozens of nanometer), the tail of evanescent field can reach the interface of guided wave layer of the metal. It will generate an opposite evanescent field on the interface. Due to the interaction between two evanescent fields from opposite directions, the incident light can be coupled into waveguide.

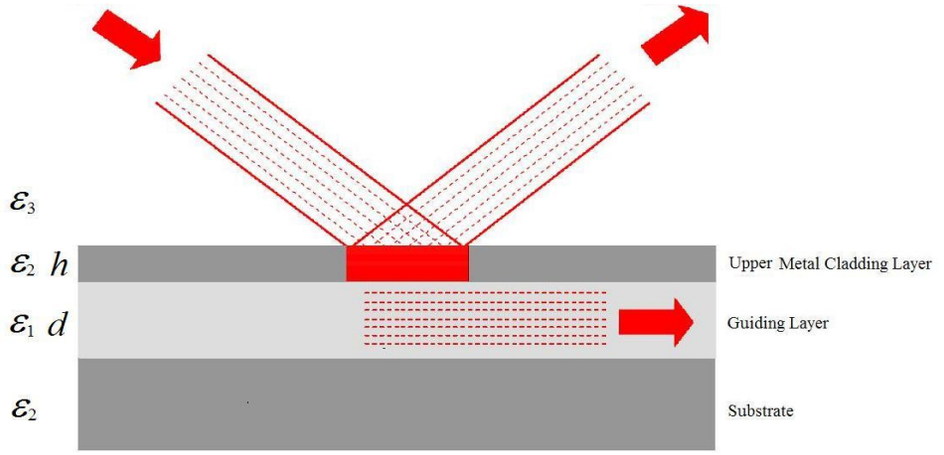

Figure 1. Symmetrical metal-cladding waveguide structure

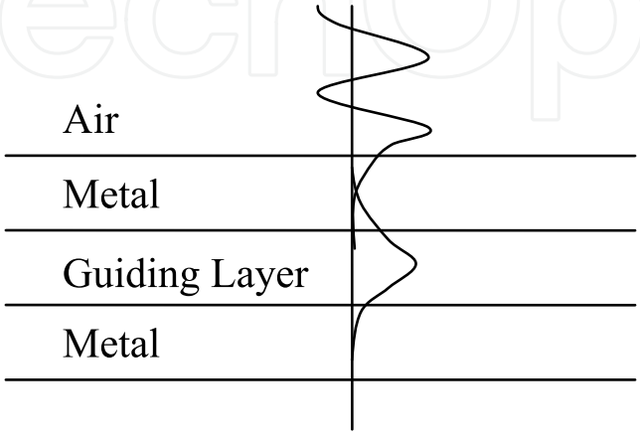

Figure 2. Principle model of free-space coupling

2.1. The attenuated total reflection spectrum

When a laser beam cast on the upper metal layer with resonant conditions, a large part of the light energy is transferred in the guiding layer, resulting in the attenuated total reflection (ATR) spectrum, which describes the relation between reflectivity and incident angle or wavelength of the reflected light. We take TE mode for example. The reflection coefficient of the four-layer optical system for TE mode is written as [7]

$$r = \frac{r_{32} - r_{32}r_{21}^2 \exp(2i\kappa_1 d) + r_{21}\exp(2i\kappa_2 h) - r_{21}\exp(2i\kappa_1 d)\exp(2i\kappa_2 h)}{1 - r_{21}^2 \exp(2i\kappa_1 d) + r_{32}r_{21}\exp(2i\kappa_2 h) - r_{32}r_{21}\exp(2i\kappa_1 d)\exp(2i\kappa_2 h)} \quad (1)$$

here $r_{ij}=(\kappa_i-\kappa_j)/(\kappa_i+\kappa_j)$, is the complex Fresnel reflection coefficient for the boundary between media i and j, in which the normal components of the wave vectors and propagation constant of guided modes are, respectively, expressed as follows:

$$\kappa_j = \sqrt{k_0^2\varepsilon_j - \beta^2}, (j = 1,2,3) \quad (2)$$

$$\beta = k_0\sqrt{\varepsilon_3}\sin\theta \quad (3)$$

here $k_0=2\pi/\lambda$ is the wavenumber in vacuum; ε_3 is the dielectric constant at medium in which the light incident and reflected; β is the propagation constant of the guided modes; θ and λ are the incident angle and wavelength, respectively. As shown in Fig.3, when the energy of the incident light is coupled into the guided modes, the intensity of the reflected light $R=|r|^2$ decreases dramatically, and a series of reflection dips in the ATR spectrum are produced.

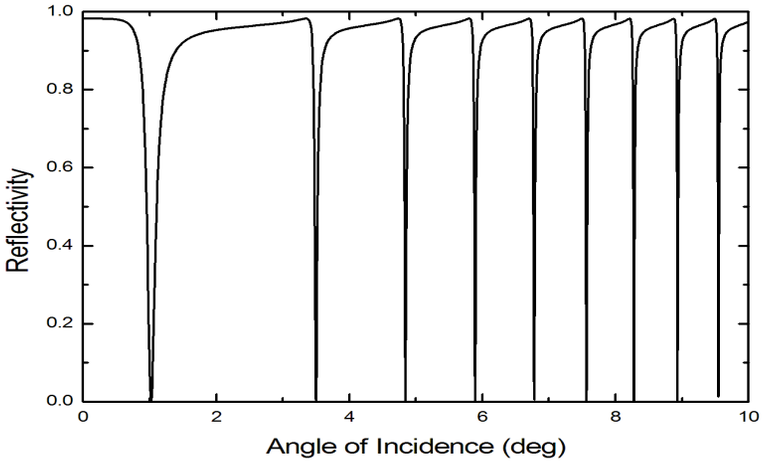

Figure 3. Simulated ATR curve with the following parameters: ε_2=-28+i1.8, ε_1=2.278, λ= 859.8nm, h=30nm, and d= 0.38mm.

The experimental arrangement for measuring ATR spectrum is shown schematically in Fig.4. The SMCW is fixed on a computer controlled $\theta/2\theta$ goniometer. After passing through the polarizer and mirror, a collimated laser light beam is incident into the structure. Angular scan is carried out by a computer-controlled $\theta/2\theta$ goniometer. As the goniometer rotates, the

incident angle will change, while the photodiode keeps consistently monitoring the reflected light intensity to scan the reflectance curve. The reflected light intensity is captured by a photodiode fixed on the 2θ plate of the goniometer and converted into a voltage signal. At small incident angles, UHM resonance will occur and couple the incident light energy into the SMCW by the free space coupling technique. Then in the reflective curve, a series of resonance dips take place in the angular spectrum, as illustrated in Fig.3.

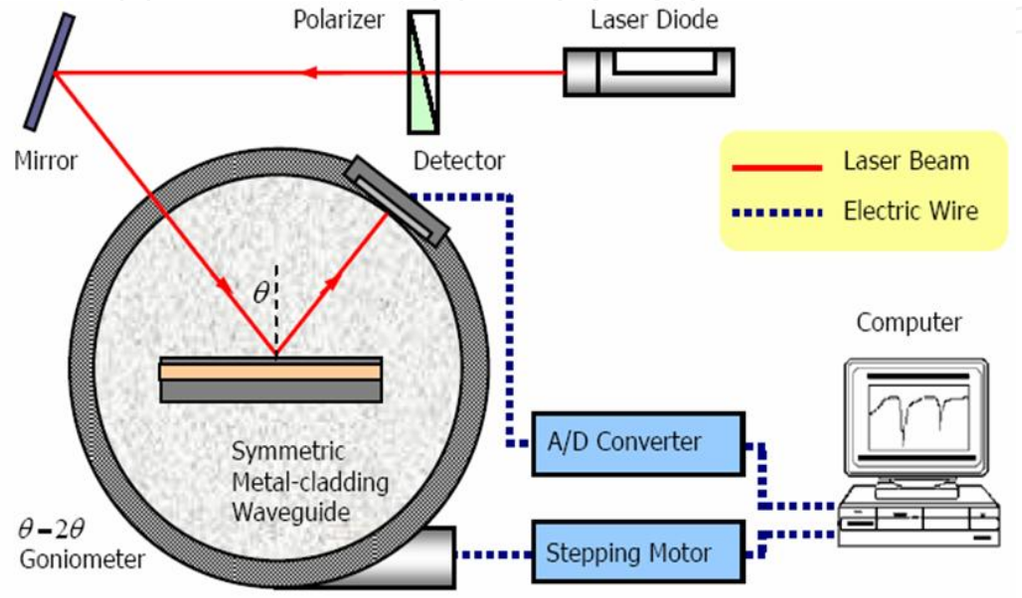

Figure 4. Experimental arrangement for measuring ATR spectrum

2.2. Ultrahigh-order mode

Disregarding the effects resulting from the limited thickness of the metal film, dispersion equation of the guided modes in SMCW can be written as

$$\kappa_1 h = m\pi + 2\tan^{-1}(\rho\frac{\alpha_2}{\kappa_1}), \quad m = 0,1,2,..... \tag{4}$$

where attenuated coefficient in the metal α_2=iκ_2, m is the mode ordinal number of guided mode. The parameters relevant to polarization are given by:

$$\rho = \begin{cases} 1 & TE\,Polarization \\ \varepsilon_1/\varepsilon_2 & TM\,Polarization \end{cases} \tag{5}$$

According to Eq. (4), we can deduce an approximate formula:

$$\Delta m \propto \sin 2\theta \Delta\theta \tag{6}$$

Since Δm=1, when the incident angle is small, a bigger $\Delta\theta$ can be obtained. So the mode spacing effect of UHMs is evident. Such property is convenient to comb filter design for optical communication applications.

Furthermore, when d reaches millimeter-scale, the waveguide can accommodate thousands of guided modes. For example, use the parameters: $\varepsilon_2 = -28 + i1.8$, $\varepsilon_1 = 2.278$, $\lambda = 859.8$nm, $h = 30$ nm, and $d = 0.38$ mm, m is 1333 for the highest mode. However, the maximum of the absolute value of the second term on the right in Eq. (4) is π. It will not generate much error if ignoring it, and the approximate dispersion equation of the UHMs for both TE and TM modes is [5]

$$\frac{2\pi}{\lambda} h \cdot \sqrt{\varepsilon_1 - N^2} = m\pi \qquad (m = 0,1,2,.....) \tag{7}$$

where $N = \beta/k_0$ is the effective index of the UHM. Eq. (7) implies that when N is close to zero, the UHM exhibits polarization insensibility.

Because UHMs have a short retention time in waveguide layer, any tiny change of λ, n_1 and d will cause the sensitive change of N. If we define sensitivity S_N as the derivative of effective index to certain characteristic parameter, that is

$$S_N = \frac{\partial N}{\partial \xi} \tag{8}$$

where ξ represents λ, n_1 or d. By the total differential of Eq. (7), we can get:

$$\frac{\partial N}{\partial n_1} = \frac{n_1}{N} \tag{9}$$

$$\frac{\partial N}{\partial \lambda} = \frac{n_1^2 - N^2}{N\lambda} \tag{10}$$

$$\frac{\partial N}{\partial d} = \frac{n_1^2 - N^2}{Nd} \tag{11}$$

From above mentioned three equations, sensitivity is in inverse proportion to effective index N. Therefore, we can obtain high sensitivity when UHM is excited. According to ray optics theory, with the same propagation distance, the small incident angle means that UHM will experience more times reflection and light propagation distance will be longer, resulting in a series of special features different from low-order modes. This property is extremely useful to design sensors and modulators.

Finally, according to Eq. (4), tiny change of wavelength can generate great change of effective index, illustrating that UHM has strong dispersion property and consequent slow light effect. Using Eq. (7), we can also obtain the group velocity of UHM:

$$v_g = \frac{d\omega}{d\beta} = \frac{N}{n_1} \cdot \frac{c}{n_1 + \omega dn_1/d\omega} \tag{12}$$

In the equation, group velocity expression is totally different from those conventional slow light schemes, which is composed of two contributions that are shown in Eq. (12): one

originates from the first-order dispersion resembling the conventional slow light system, and factor N/n_1 can be called slow light factor which is related to the effective index of the UHMs. The deduced results offer us a new physical mechanism for realizing slow light that may not rely on the existence of a sharp single resonance or multiple resonances, but the effective index of the UHM for the small incident angle ($\theta \to 0$).

2.3. Propagation loss

Once SMCW is used to achieving optical devices, the important concern relating to the SMCW is that metallic structures exhibit high losses at optical wavelengths. An issue arising is whether the UHMs could be efficiently confined to the guiding layer over a long distance transmission. To see this clearly, four types of metal cladding waveguides have been considered as shown in Fig.5. Fig.5(a) is a structure of three-layer metal cladding waveguide without considering metal and radiative loss. By using three-layer waveguide theory, for TE mode, propagation constant, β^a, of guided modes for three-layer metal cladding waveguide without considering the metal absorption, can be expressed as:

$$\beta^a = \frac{\pi}{\lambda d}\sqrt{4\varepsilon_1 d^2 - (\mathrm{m}_0\lambda)^2} \tag{13}$$

where m_0 is mode order.

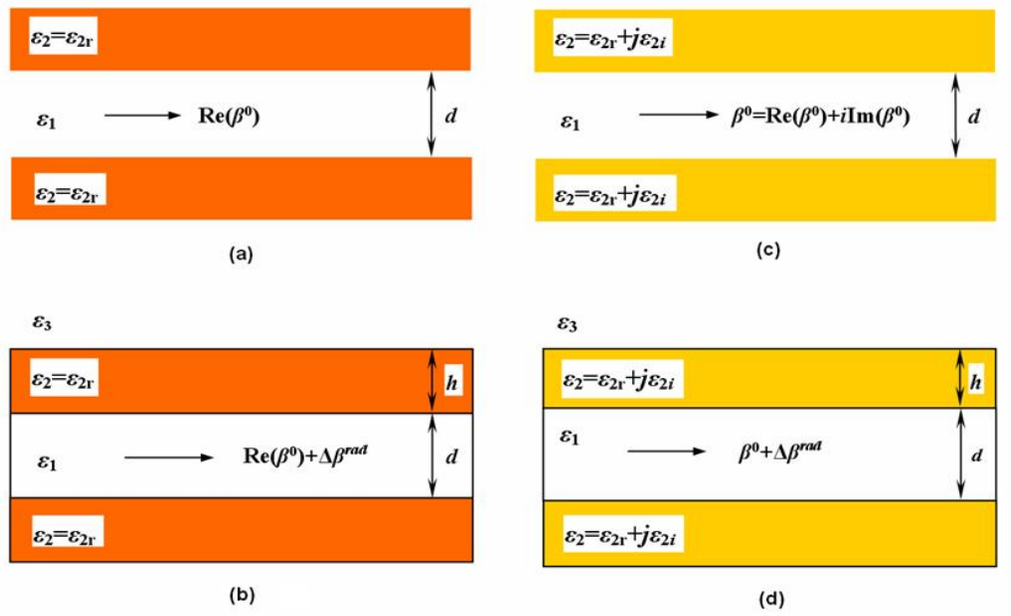

Figure 5. (a) three-layer metal cladding waveguide with $\varepsilon_2=\varepsilon_{2r}$ and $h\to\infty$, (b) SMCW with $\varepsilon_2=\varepsilon_{2r}$ and $h \neq \infty$, (c) three-layer metal cladding waveguide with $\varepsilon_2=\varepsilon_{2r}+i\varepsilon_{2i}$ and $h\to\infty$, (d) SMCW with $\varepsilon_2=\varepsilon_{2r}+i\varepsilon_{2i}$ and $h \neq \infty$.

Fig.5(b) is a structure of SMCW only with considering radiative loss. Comparing Fig.5(b) with Fig.5(a) by using weak-coupling condition, which is satisfied with four-layer system [8], the radiative damping, $\mathrm{Im}(\Delta\beta^{\mathrm{rad}})$, can be expressed as,

$$\mathrm{Im}(\Delta\beta^{rad}) = \frac{4\alpha_2^a(\kappa_1^a)^2\kappa_3^a \exp(-2\alpha_2^a h)}{((\kappa_1^a)^2+(\alpha_2^a)^2)((\kappa_3^a)^2+(\alpha_2^a)^2)\beta^a d_{eff}} \tag{14}$$

with

$$\kappa_1^a = \sqrt{k_0^2\varepsilon_1 - (\beta^a)^2} \tag{15}$$

$$\alpha_2^a = \sqrt{(\beta^a)^2 - k_0^2\varepsilon_{2r}} \tag{16}$$

$$\kappa_3^a = \left(k_0^2\varepsilon_3 - \left(\beta^a\right)^2\right)^{1/2} \tag{17}$$

and

$$d_{eff} = d + 2/\alpha_2^a \tag{18}$$

Where α_2^a is the absorption constant of the cladding layer, κ_1^a is the vertical guiding wave vector of three-layer metal cladding waveguide without considering the metal absorption, ε_{2r} and ε_{2i} are real and imaginary parts of dielectric constant ($\varepsilon_2=\varepsilon_{2r}+j\varepsilon_{2i}$), and d_{eff} is the effective thickness. $\Delta\beta^{rad}$ represents the difference of the eigen-propagation constant between three-layer waveguide and radiative waveguide coupling system. Because the radiative damping is inversely proportional to the exponential function of h as shown in Eq. (14), the radiative damping can be adjusted by changing the parameter h.

Fig.5(c) is a structure of three-layer metal cladding waveguide only with considering metal loss. Comparing Fig.5(a) with Fig.5(c) under the condition of $|\varepsilon_{2r}|>>\varepsilon_{2i}$ at visible and near infrared wavelength, we can obtain that metal loss only affects the imaginary part of propagation constant in three-layer metal cladding waveguide. Then the intrinsic damping, $\mathrm{Im}(\beta^0)$, can be written as [8]:

$$\mathrm{Im}(\beta^0) = \frac{\varepsilon_{2i}k_0^2(\kappa_1^a)^2}{\alpha_2^a((\kappa_1^a)^2+(\alpha_2^a)^2)\beta^a d_{eff}} \tag{19}$$

where β^0 is the eigen-propagation constant of the guided mode for three-layer waveguide with semi-infinite-thick coupling layer. Table1 lists the propagation loss of two kinds of SMCW which thickness of guiding layer d is 0.5 mm and 1 mm, corresponding to UHM order m is 1421 and 2843, separately. The dielectric constant of Au and Ag at wavelength λ= 1053 nm is -40+2.5i and -48+1.6i, respectively. η presents the ratio of the remaining power after the guided mode transmits for z= 1 mm to the guided mode initial power and can be expressed as $\exp(-2\Delta\beta z)$. Then the propagation loss ζ can be expressed as $-10/z\times lg\eta$. As shown in table 1, in sub-millimeter scale, the propagation losses of the guided modes are both less than 3 dB/mm, which is benefit for the design of optical devices. In addition, the propagation loss property has little relation to polarization.

h/mm	λ/nm	ε	m	mode	|Δβ|	η/%	ζ/(dB/nm)
0.5	1053	εAn=-40+2.5i	1421	TE	0.31904	52.8	2.78
0.5	1053	εAn=-40+2.5i	1421	TM	0.32289	52.4	2.81
0.5	1053	εAg=-48+1.6i	1421	TE	0.15689	73.1	1.36
0.5	1053	εAg=-48+1.6i	1421	TM	0.15834	72.9	1.38
1	1053	εAn=-40+2.5i	2843	TE	0.15953	72.7	1.38
1	1053	εAn=-40+2.5i	2843	TM	0.16144	72.4	1.4
1	1053	εAg=-48+1.6i	2843	TE	0.078446	85.4	0.69
1	1053	εAg=-48+1.6i	2843	TM	0.079167	85.3	0.7

Table 1. Guided-mode propagation loss with different parameters

2.4. The enhanced Goos–Hänchen effect

When the weak coupling condition $|\exp(2i\kappa_2 h)|<<1$ is satisfied, Eq. (1) can be rewritten as

$$r = |r|e^{i\phi} = r_{32}\frac{\beta - \left[\mathrm{Re}\left(\beta^0\right)+\mathrm{Re}\left(\Delta\beta^{rad}\right)\right] - i\left[\mathrm{Im}\left(\beta^0\right)-\mathrm{Im}\left(\Delta\beta^{rad}\right)\right]}{\beta - \left[\mathrm{Re}\left(\beta^0\right)+\mathrm{Re}\left(\Delta\beta^{rad}\right)\right] - i\left[\mathrm{Im}\left(\beta^0\right)+\mathrm{Im}\left(\Delta\beta^{rad}\right)\right]} \tag{20}$$

where φ is the phase difference between the reflected and incident waves. Re(β^0), Im(β^0) and Re($\Delta\beta^{rad}$), Im($\Delta\beta^{rad}$) are the real and imaginary parts of the parameters β^0 and $\Delta\beta^{rad}$, respectively.

According to stationary phase method, the Goos-Hänchen (GH) shift L is expressed as:

$$L(\lambda) = -\frac{\lambda}{2\pi\sqrt{\varepsilon_3}}\cdot\left.\frac{d\phi}{d\theta}\right|_{\theta=\theta_0} \tag{21}$$

where θ_0 is the fixed incident angle. Using (20), L at the resonance wavelength of ATR curve can be written as [9]

$$L(\lambda_{res}) = -\cos\theta_0\cdot\frac{2\,\mathrm{Im}(\Delta\beta^{rad})}{\mathrm{Im}(\beta^0)^2-\mathrm{Im}(\Delta\beta^{rad})^2} \tag{22}$$

With the parameters ε_3=1, ε_1=2.278, ε_2=-28+1.8j, θ_0=8.11, d=0.38μm, and h=22nm, the calculated GH shifts with respect to wavelength is shown in Fig.6. The reflectivity is also shown in Fig.6 for comparison. It is found from Fig.6 that the enhancement of the lateral shift of reflective light is closely relevant to the coupling of waveguide power. Reflectivity corresponds to the excitation of a guided mode with the change of the incident wavelength. When the incident wavelength gradually meets the condition of resonance, the reflectivity decreased sharply, most of the energy of the incident angle is coupled into waveguide, greatly enhance the reflective GH shift and forms a peak, and this peak of lateral shift corresponds to the minimum of the reflectivity. Moreover, as the radiative damping is inversely proportional to the exponential function of h from Eq. (14), we can adjust radiative damping by varying h. When h

is small, the radiative damping is larger than the intrinsic damping, positive lateral shift is obtained. The negative GH shift corresponds to the reverse case. Larger GH shift can be obtained when intrinsic damping approaches the radiative damping. The critical thickness can be determined from Eq. (22) by letting denominator is equal to zero [8]:

$$h_{cr} = \frac{\lambda}{4\pi\kappa} \ln \frac{2}{n} \tag{23}$$

where n and κ are the refractive index of the metal ($n+j\kappa=(\varepsilon_2)^{1/2}$). The critical thickness should be about 31nm using the parameters above.

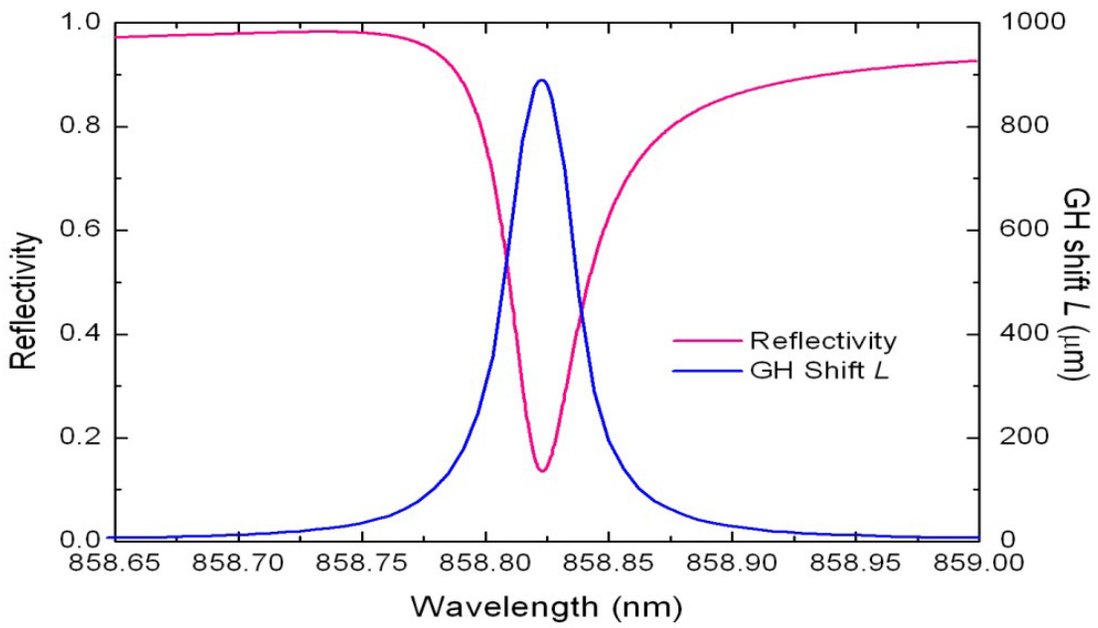

Figure 6. Reflectivity and lateral beam shift with respect to the incident wavelength

To measure the shift while avoiding small spurious displacement, we use the wavelength interrogation-based method by combining a tunable laser and a one-dimensional position sensitive detector (PSD). The position of the incident light can be determined by the PSD through the photocurrents from the output electrodes x_1 and x_2 (see Fig.7):

$$\Delta L = \frac{a}{2}\delta \tag{24}$$

where ΔL is the displacement from the center of the PSD, a is the length of the PSD, δ is defined as

$$\delta = \frac{I_1 - I_2}{I_1 + I_2} = \frac{V_1 - V_2}{V_1 + V_2} \tag{25}$$

here I_1 and I_2 are the photocurrents of the output electrodes x_1 and x_2, respectively. V_1 and V_2 are the voltages converted from I_1 and I_2 after amplifier circuit. The analog voltages V_1 and V_2 are further converted into digital signals and collected by the computer (PC). Light

displacement measurement using PSD can achieve high sensitivity and accuracy and will not be affected by the change of the light intensity.

The experimental arrangement for measuring GH shift is shown in Fig.7 [10]. After passing through two apertures (A_1, A_2) and a splitter (S_1), a large part of the Guassian beam from a tunable laser was introduced onto the SMCW. Another part of the beam, which is reflected from S1, irradiated the second splitter (S_2) and is detected by a wavemeter connected to a computer. We choose to excite the UHMs, because of the polarization independence of the UHMs, TE and TM incidences have nearly the same characteristics. The reflected light from the SMCW was first detected by a photodiode (PD). Angular scan was performed by rotating the goniometer and the ATR spectrum was generated. We selected the operation angle to be located at the maximum reflectivity near a certain dip of the spectrum (Position 1). The GH effect is not remarkable at this position due to the deviation of the resonance condition. The position of the reflected beam was set as the reference at this point. Then we moved the PD out of the light path (Position 2) without changing any position of the incident beam and let the reflected light beam cast onto the center of the PSD perpendicularly. Then by changing the wavelength through temperature tuning, the variation of δ can be measured obviously on the computer screen. To gain better understanding of GH shift measurement using PSD, Fig.8(a) and (b) show the two sets of measurement results when the wavelength of the incident light is changed artificially. The values of V_1 and V_2 are also measured and plotted in the two figures for comparison. Since the preliminarily setting of the light is at the center of PSD under the case of unresonance, which means the reference values of δ is equal to zero, the change of the value δ shown on the computer were the actual relative enhanced positive and negative lateral beam displacement under the case of resonance. Then the actual position ΔL can be obtained by using Eq. (24).

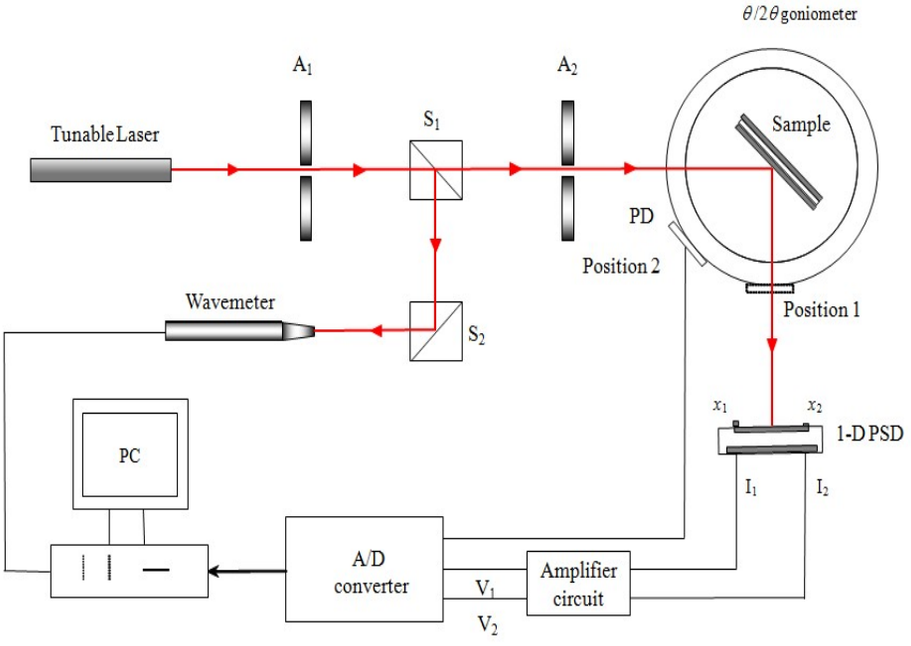

Figure 7. Experimental setup (A_1 and A_2, aperture; PD:photodiode; S_1 and S_2: splitter; 1-D PSD: one-dimensional position sensitive detector and PC: computer).

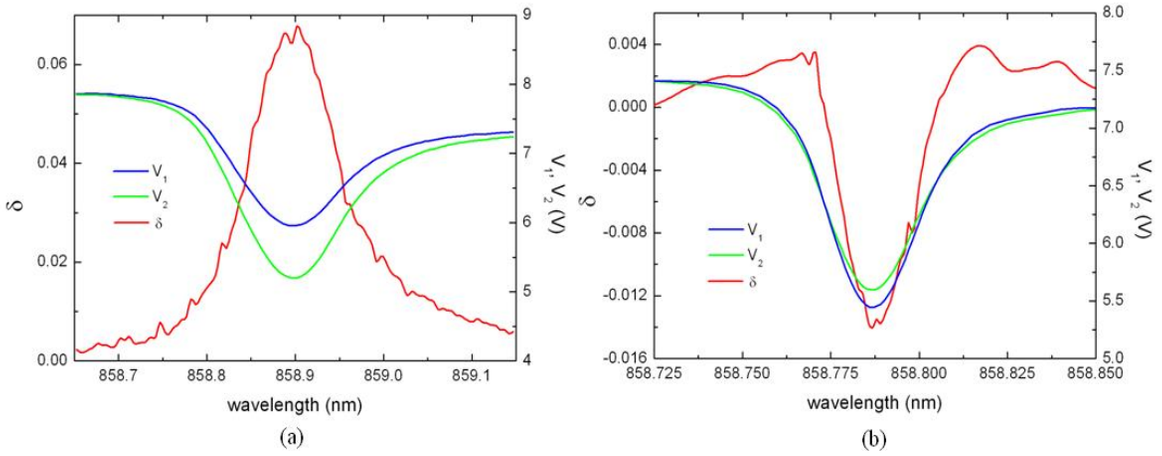

Figure 8. Measured analog voltages V_1 and V_2 and calculated positive value of δ as a function of wavelength with (a) h=8nm and (b) h=50nm. The incident angle θ is 8.11°.

3. Optical devices based on SMCW

The above mentioned properties of UHM in SMCW have been widely used to applications on optical devices. Here, we list several practical application examples, such as filter, sensor, modulator and slow wave device. Due to its excellent performance and simple structure, optical devices based on SMCW have the potential applications in many fields.

3.1. Tunable comb filters

As mentioned above, a sub-millimeter SMCW is capable of coupling the incident light with a fixed wavelength from free space into the glass slab directly. As the excitation of the guided modes results in resonant transfer of energy from the incident light, guided modes manifest themselves by a series of resonant dips in the reflectivity when the incident angle is varied. On the other hand, if a polychromatic light is used instead of a single-wavelength light, resonant dips at a fixed incident angle can also be achieved in a spectral plot of the reflectivity. In this way, a comb filter is built [11]. For a better understanding of how it works, we consider the UHMs of the sub-millimeter SMCW in the case of free space coupling. Eq. (7) can be rewritten as

$$\frac{2\pi\nu}{c} n_1 d\cos\theta = m\pi \tag{26}$$

where ν is the frequency of the light in free space. Without considering the material dispersion of the waveguide, we can express the channel spacing in frequency separated by two neighboring guided modes as

$$\Delta\nu = \frac{c}{2n_1 d\cos\theta} \tag{27}$$

It is found that θ is a constant as the incident angle of the light is fixed, which means that the channel spacing is equal in frequency for this comb filter. Moreover, according to Eq. (26)

and (27), both the center wavelength and the channel spacing can be tuned by simply changing the incident angle. The parameters of SMCW that achieve comb filter are as follows: a glass (ZF7) slab (d=900μm); the thickness of the upper film h=20 nm. Fig.9 shows the output spectrum from the SMCW.

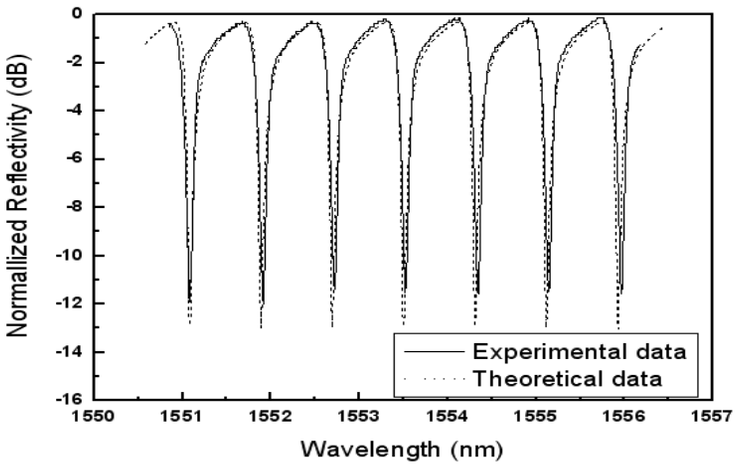

Figure 9. Experimental and theoretical reflective spectrum of SMCW, with parameters $\varepsilon_2 = -132 + i12.56$, $n_1 = 1.765$, $h = 21$ nm, $d = 0.85$ mm and $\theta = 6.1^o$

From Fig.9, we can see equally spaced loss peaks with a 3 dB line-width of 0.1 nm appear in the spectral plot from 1551 to 1556 nm. The wavelength spacing of these peaks is just 0.8 nm. The channel isolation, which is closely related to the thickness of the upper gold film of the waveguide, has been found to be 12 dB. Insertion loss is characterized by the maximum reflectivity, which is greater than 95% (~0.2 dB). The tunability of the filter can be obtained simply by slightly rotating the waveguide with respect to the incident light. Tuning of the center wavelength in the range of channel spacing can be easily obtained by changing several degrees of the incident angle according to Eq. (26).

3.2. Optical sensors

In this section, we propose oscillating wave sensors using SMCW structure. The thickness of guiding layer can be expanded to millimeter scale, which it can contain very sensitive UHM. The high sensitivity can be detected by measuring the intensity variation of the reflected light due to the movement of the corresponding synchronous angle by an optical sensor. In addition, an alternative approach is presented via measuring the enhanced GH shifts at excitement of UHM. This approach enables the possibility to obtain a higher resolution and prevent the disturbance caused by the power fluctuation of the light source.

3.2.1. Sensitivity analysis

If we using the intensity measurement interrogation to observe the response of the sensor, the sensitivity in SMCW can be defined as the rate of change of the reflectivity to center characteristics parameters which is expressed as:

$$S_I = \frac{dR}{d\xi} = \left(\frac{\partial R}{\partial \theta}\right)\left(\frac{\partial \theta}{\partial N}\right)\left(\frac{\partial N}{\partial \xi}\right) \tag{28}$$

Using the phase matching condition of resonance energy transfer, the effective refractive index N can be expressed as

$$N = \sqrt{\varepsilon_3}\sin\theta \tag{29}$$

Combined (28) with (29), the sensitivity S_I can be written by

$$S_I = \left(\frac{\partial R}{\partial \theta}\right)\left(\frac{\partial \theta}{\partial N}\right)\left(\frac{\partial N}{\partial \xi}\right) = \frac{1}{\sqrt{\varepsilon_3}\cos\theta}\left(\frac{\partial R}{\partial \theta}\right)\left(\frac{\partial N}{\partial \xi}\right) \equiv \frac{1}{\sqrt{\varepsilon_3}\cos\theta} S_R S_N \tag{30}$$

where S_N is defined as the rate of change of the effective refractive index N with respect to certain characteristic parameter and determined by Eq.(9)-(11). As described in section 2.2, optical waveguide oscillating field sensor exhibits the substantial improvement: the UHMs of the SMCW with millimeter scale is selected to act the sensing probe, so $N \to 0$ and S_N enhancement has been achieved. S_R represents the slope of the dip at the operation angle θ_0, which was usually set at the fall-off side. The absolute maximum values of the slopes are related to the width of the ATR reflection dips and the mode number. The larger the mode number, the wider the corresponding ATR dip, and the smaller the steepest slope. So the divergence angle of the incident light should be taken into consideration. To calculate the maximum value of sensitivity S_I, Lorentzian function is used to approximate the reflection dip in the ATR spectrum. The FWHM is assumed to be larger than the divergence of the incident light in order to prevent profile distortion. According to Ref [12], S_R can be expressed as

$$S_R = \frac{\partial R}{\partial \theta} = \frac{4(R_0 - R_m)}{\alpha\sqrt{2\pi}} \int_{-\infty}^{\infty} \left[\frac{2Q^2}{(x - x_0)^2 + 2Q^2}\right] \cdot x \exp(-x^2) dx \tag{31}$$

with

$$Q = W / \alpha \tag{32}$$

$$x = \sqrt{2}(\theta_i - \theta) / \alpha \tag{33}$$

$$x_0 = \sqrt{2}(\theta_i - \theta_{sp}) / \alpha \tag{34}$$

where R_m and R_0 are the values of the reflectivity when guided mode is and is not excited, respectively. θ_{sp} is the angle for exciting the guided mode, W is the half of the FWHM of the dip, and α is the divergence half-angle of the laser beam.

Taking wavelength sensing for example [13], use the parameters: $\varepsilon_2 = -28 + i1.8$, $\varepsilon_1 = 2.278$ at 859.8 nm, h = 30 nm, α = 0.4 mrad and d = 0.38 mm. The sensitivity S_I with respect to the

angle of incidence is shown in Fig.10. The UHMs are more sensitive than the low-order modes and are more applicable for sensing.

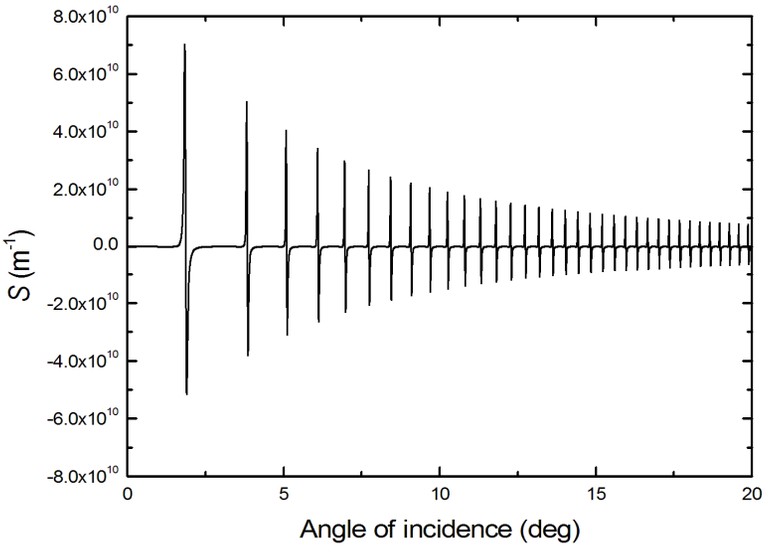

Figure 10. S_I versus incident angle θ

Similarly, in the GH shift interrogation, the sensitivity of the sensor is defined by the change rate of the GH shift (L) with respect to center characteristics parameters and it can be written as

$$S_{GH} = \left(\frac{\partial L}{\partial \theta}\right)\left(\frac{\partial \theta}{\partial N}\right)\left(\frac{\partial N}{\partial \xi}\right) = \frac{1}{\sqrt{\varepsilon_3}\cos\theta}\left(\frac{\partial L}{\partial \theta}\right)\left(\frac{\partial N}{\partial \xi}\right) \equiv \frac{1}{\sqrt{\varepsilon_3}\cos\theta} S_L S_N \tag{35}$$

Compared with the intensity interrogation, the only difference is the replacement of S_R by S_L. According to Eq. (22), if the intrinsic damping of the UHM is close to the radiative damping, a large GH shift can be observed [10]. The dependence of the GH shift on the effective index for a selected mode forms a resonance peak. High sensitivity S_{GH} can be reached at the up and down sides of the peak. In addition, since the magnitude of the GH shift is irrelevant to the incident light intensity, a power fluctuation of the laser brings no disturbance to the resolution of the optical sensor.

Moreover, the thickness of the upper metal cladding is also an important factor that must be considered when analyzing the sensitivity. The thicknesses of upper and bottom metal films are essential parameters in the determination of the sensitivity. If thickness h is excessively thick, it is difficult for the incident light power to be coupled into the planar waveguide structure. However, if thickness h is too thin, it is easy for the incident energy to be coupled into the waveguide. On the other hand, it is also easy for the light energy to be coupled out of the waveguide. As a consequence, there is an optimum solution to thickness h by which the highest sensitivity is obtained. Theoretical and experimental results show that the optimal thickness for the upper metal layer is within the range of about 31–33 nm if the maximum sensitivity is to be achieved. In the following section, refractive index (RI), displacement and light wavelength sensing with extremely high sensitivity are introduced.

3.2.2. Refractive index sensing

In the intensity interrogation (as illustrated in Fig. 11(a)), the sample is sealed by an O-ring sandwiched between two gold films that deposited on glass substrates. The two gold films and the sample cell form the SMCW structure. The upper gold film (35 nm in thickness) is deposited on a thin glass slide. The glass slide is 0.178 mm in thickness, with a RI of 1.50. The lower gold film (300 nm) is deposited on a glass plate. The lower glass plate's thickness is 2 mm with an RI of 1.50. The dielectric constants of the gold films are −11.4+i1.50 at the wavelength of 650 nm. The sample cell serves as the guiding layer of the waveguide sensor, and the thickness of the sample cell is governed by the thickness of the O-ring of about 1.99 mm. The aqueous sample could be pumped in and out of the sample cell by a peristaltic pump through the inlet and outlet on the lower substrate. The water sample with an RI of 1.333 can be used as the guiding layer of the waveguide. The guided wave concentrates and propagates in the sample layer as the oscillating field and hence a magnification in sensitivity is expected. Fig.11(b) is the sensor sample [14].

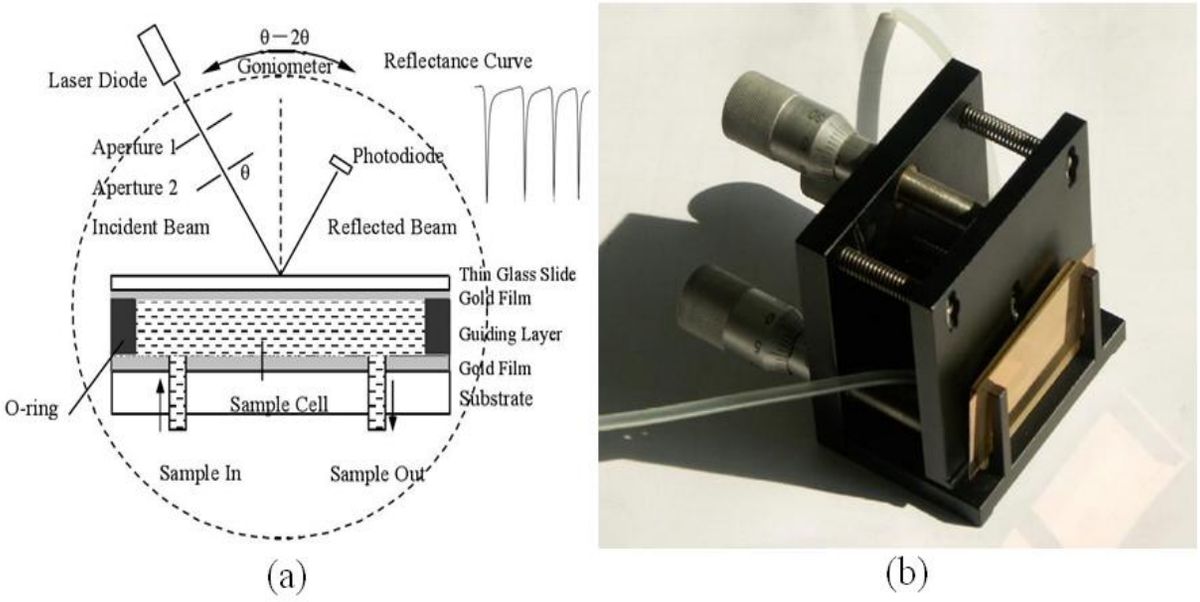

Figure 11. RI sensor of intensity interrogation (a) structural sketch; (b) actual picture

Based on sensitivity analysis, S_I can be cast in the form of

$$S_I = \frac{1}{\sqrt{\varepsilon_3}\cos\theta}\left(\frac{\partial R}{\partial \theta}\right)\left(\frac{\partial N}{\partial n_1}\right) \equiv \frac{S_R n_1}{\cos\theta \cdot \sin\theta} \tag{36}$$

Then we can see that the use of a smaller incident angle (1.69° in the experiment) as a sensing probe can achieve higher sensitivity. The experimental results are shown in Fig.12. In this case, a 20 ppm NaCl concentration change (corresponding to 2.6×10^{-6} RIU) can cause a reflectance change of around 3%.With a standard error of 0.2% for the measurement of the optical intensity[15], its resolution with 1% noise level can reach up to 0.88×10^{-6} RIU for the ideal case.

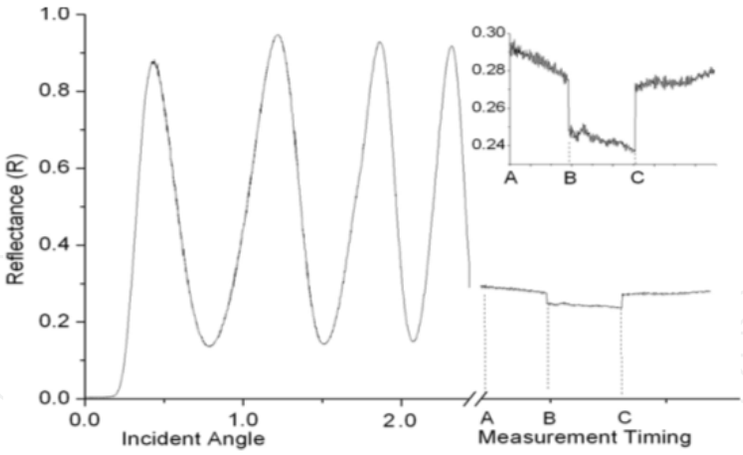

Figure 12. Sensor response for NaCl water solution in the experiment. The left side of the curve is the scanned reflectance curve of the three highest guiding modes. The scan motor stopped at the fall-off of the fourth resonance dip. 20 ppm NaCl water solution is filled in the sample cell and the first measurement starts at A and is then paused. After pure water is pumped in the sample cell and the signal stabilized, measurement starts at B and then back to the 20 ppm NaCl sample measurement at C. The sensor response is enlarged in the inset.

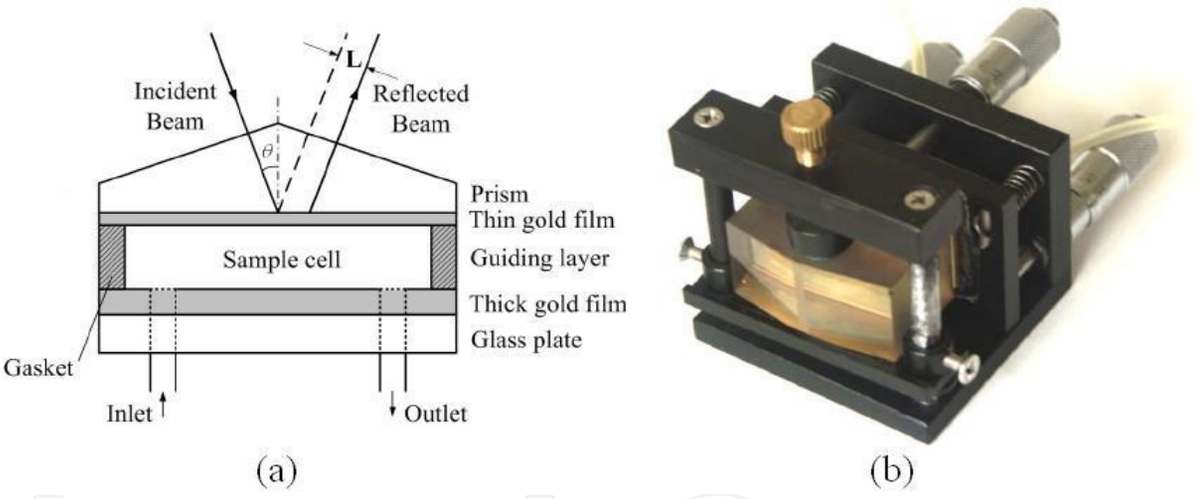

Figure 13. RI sensor of GH shift interrogation (a) structural sketch; (b) actual picture

In the GH shift interrogation (as illustrated in Fig. 13), a glass prism is coated with a 20 nm thick gold film to serve as the coupling layer. A 300 nm thick gold film is sputtered on a glass slab to act as the substrate. The air gap of 0.7 mm sandwiched between two gold films works as the guiding layer, where a gasket is used to form a sealed sample cell. With the help of a peristaltic pump, sample liquids to be detected flow into the cell through the inlet and the outlet tubes embedded in the substrate glass plate.

The expression of sensitivity S_{GH} is similar to Eq. (36) by replacing S_R with S_L. So UHM is also selected as a sensing probe. Experiments are carried out with the waveguide parameters as follows: θ=4.60°, ε_3=2.25, ε_2=−28+1.8i, h=20 nm, and d=0.7 mm, for pure water (solid curve), n_1=1.333 RIU. A series of NaCl solutions with the change step of 20 ppm in concentration is used as sample analyte to be probed. The experimental result is shown in

Fig.14. The step change of 20 ppm NaCl solution in concentration, which corresponds to a variation of 2.64 ×10^{-6} RIU, induces a GH shift change of at least 20 μm. Considering the noise level in the experiment, the probing sensitivity of 2.0×10^{-7} RIU is resolved since the measurement variation of the GH shift is confined within 1.5 μm for each sample [16].

3.2.3. Displacement sensing

In the experimental setup, we propose to use a variable air gap produced by a calibrated piezoelectric translator (PZT) to act as the guiding layer of the optical waveguide. As shown in Fig.15, the sample for minute displacement measurement is composed of two parts: one is a glass prism on its base precoated with a thin gold film; the other is a 500 μm thick LiNbO3 slab sandwiched between two 400 nm thick gold films and serves as a PZT. The two components, separated by an air gap with a thickness of 100 mm, are rigidly mounted on a heavy platform. The gold films deposited on the prism and the upper surface of LiNbO3 slab, together with the air gap form an SMCW.

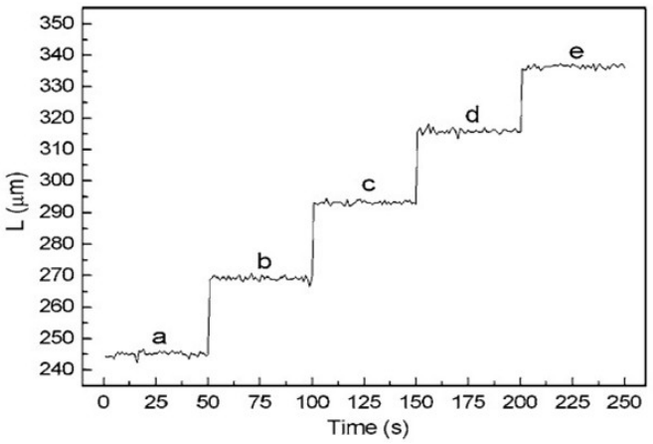

Figure 14. The GH shifts with respect to solutions of different concentrations in the sample cell: (a) pure water, (b) 20ppm NaCl solution, (c) 40 ppm NaCl solution, (d) 60 ppm NaCl solution, and (e) 80 ppm NaCl solution

As soon as applying a dc voltage on the pair electrodes of the PZT, the air gap changes its thickness due to the piezoelectric effect of the LiNbO3 slab. As a result, the reflection dip shifts its peak position and result in a change of the reflectivity. According to the resolution of the reflectivity variation, displacement can be evaluated from the applied voltage and the piezoelectric coefficient of the LiNbO3 slab. In the intensity interrogation, S_I can be cast in the form of

$$S_I = \frac{1}{\sqrt{\varepsilon_3}\cos\theta}\left(\frac{\partial R}{\partial \theta}\right)\left(\frac{\partial N}{\partial d}\right) \equiv \frac{\varepsilon_1 - \varepsilon_3 \sin^2\theta}{\varepsilon_3 \cos\theta \cdot \sin\theta \cdot d} \cdot S_R \tag{37}$$

We can also use UHM as the sensing probe to achieve higher sensitivity. Test experiment has been performed with the waveguide parameters as follows: ε_1=1.0, ε_2=−11+i1.0, ε_3=3.0, d=108 μm, h=40 nm, and λ=650 nm. Displacement sensitivity of proposed configuration is

shown in Fig.16. The waveguide thickness d is increased and decreased in steps by increasing and reducing the voltages applied on the electrodes of the PZT. The step-style change of voltage is 50 V. According to the piezoelectric coefficient of a Z-cut LiNbO3 slab, d_{33}=33.45 pm/V, the value of the displacement resolution for the proposed configuration is determined as S_I =50×33.45×10^{-3}=1.7 nm, which corresponds to the reflectivity change of R=1%[17].

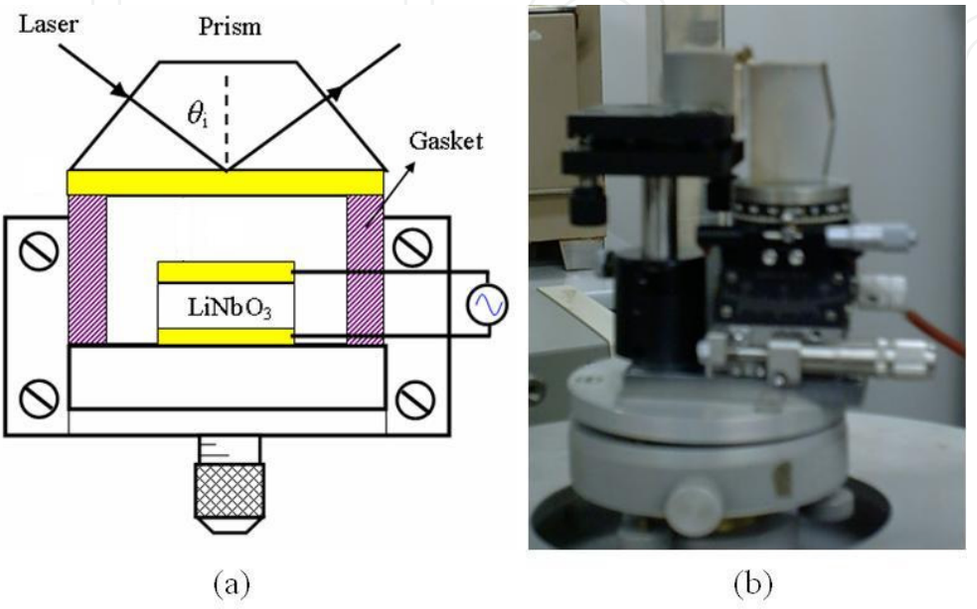

Figure 15. Displacement sensor of intensity interrogation (a) structural sketch; (b) actual picture

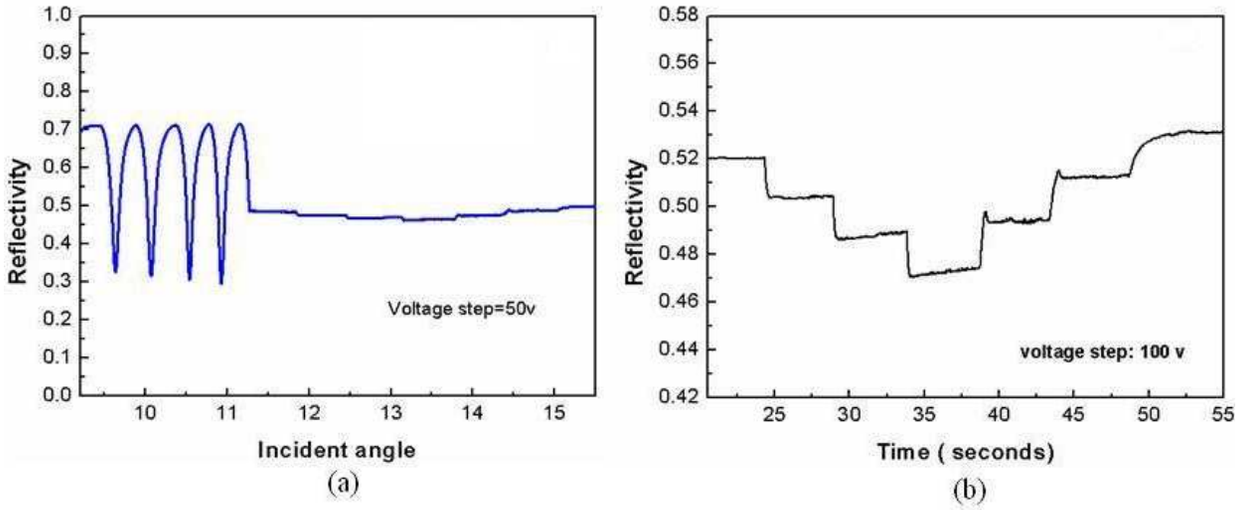

Figure 16. Experimental result of displacement measurement: (a) m-line obtained by angular scanning and displacement experimental result; (b) intensity export by applying step-styled voltages.

In the GH shift interrogation, the sensor structure is the same as Fig. 15. The experiment was performed with the following parameters: ε_2=−28+1.8i, ε_1=1, ε_3=2.25, d=500 μm, and h =18 nm. The incident wavelength is adjusted to be 859.00 nm. The experimental result is shown in Fig.17. The voltage applied on the PZT between each step is 10 V, and the piezoelectric

coefficient of the z-cut LiNbO3 is d_{33}=8 ×10^{-12} m/v. Thus, the thickness change per step is determined as Δd=8×10^{-12}×10 m=8×10^{-11} m, which leads to a GH shift change of 2 μm. The experimental ripple of each step is confined to 0.5 μm. With this noise level, the sensing resolution is evaluated to be 40 pm[18].

3.2.4. Wavelength sensing

In the intensity interrogation, the wavelength sensitivity S_I can be written as

$$S_I = \frac{1}{\sqrt{\varepsilon_3}\cos\theta}\left(\frac{\partial R}{\partial \theta}\right)\left(\frac{\partial N}{\partial \lambda}\right) \equiv \frac{\varepsilon_1 - \varepsilon_3 \sin^2\theta}{\varepsilon_3 \cos\theta \cdot \sin\theta \cdot \lambda} \cdot S_R \tag{38}$$

It is found that the effective index is extremely sensitive to λ in the case of $N \rightarrow 0$. The waveguide parameters are given as follows: d = 0.38 mm, ε_2 = −28 + i1.8, ε_1 = 2.278, and h= 31 nm. The initial wavelength was set to 859.800 nm. Once this value was stabilized, the reference wavelength was changed subsequently to 859.8005, 859.8010, 859.8015, and 859.8020 nm and decreased back to 859.8000 nm in steps. The step-style change of wavelength is 0.5 pm, with the average 2.5% change in the reflectivity ΔR. Considering a noise level of about 0.05% in Fig.18, a resolution of 0.2pm is finally obtained for the reflectivity change of R=1%[13].

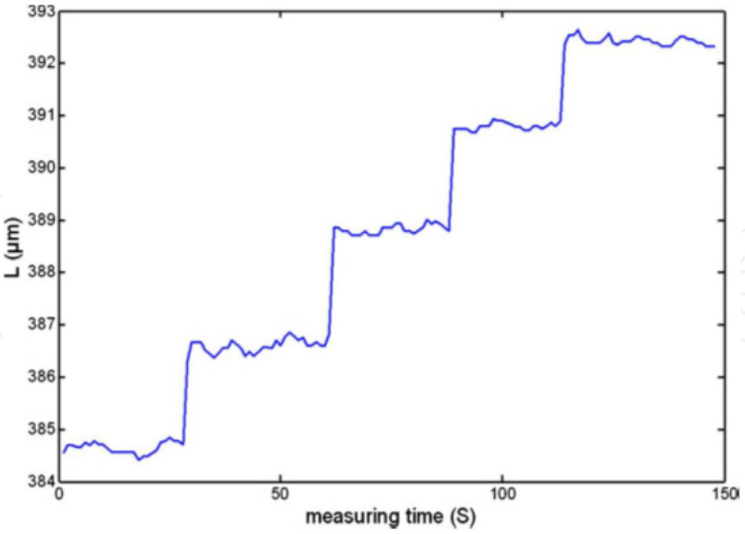

Figure 17. Experimental sensitivity of the proposed configuration. Voltage applied on the PZT between each step is 10 V, which leads to an 8×10^{-11} m change of the air gap thickness.

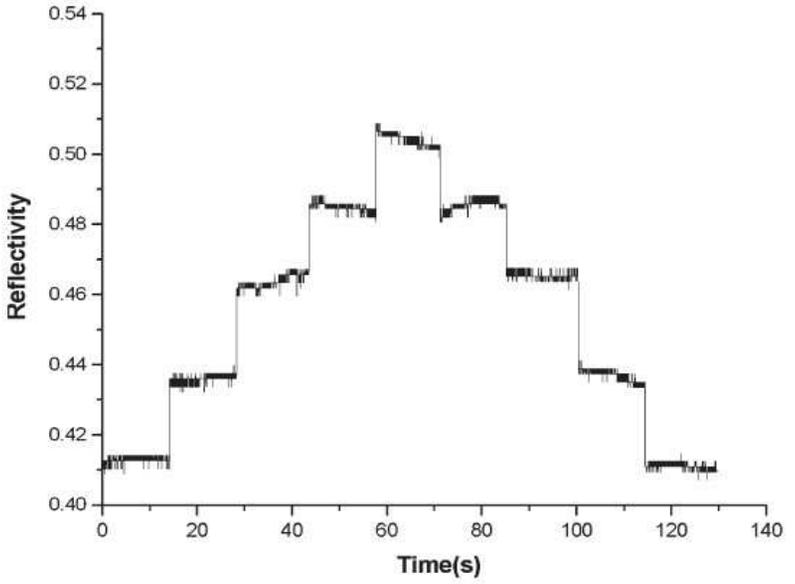

Figure 18. Wavelength sensitivity of the proposed configuration. The shift in the ATR curve was measured by changing the wavelength in steps of 0.5 pm. The angle of incidence is 3.82°.

For the GH shift measurement, the waveguide parameters are given as follows: d = 0.5 mm, ε_2 = −28 + i1.8, ε_1 = 1, ε_3 =2.25, h = 19.8 nm, and θ=4.263°. We first fix the wavelength (λ=859.003 nm). As shown in Fig.19, the change of wavelength 1 pm will cause the average variation of reflective light lateral shift about 10 μm.

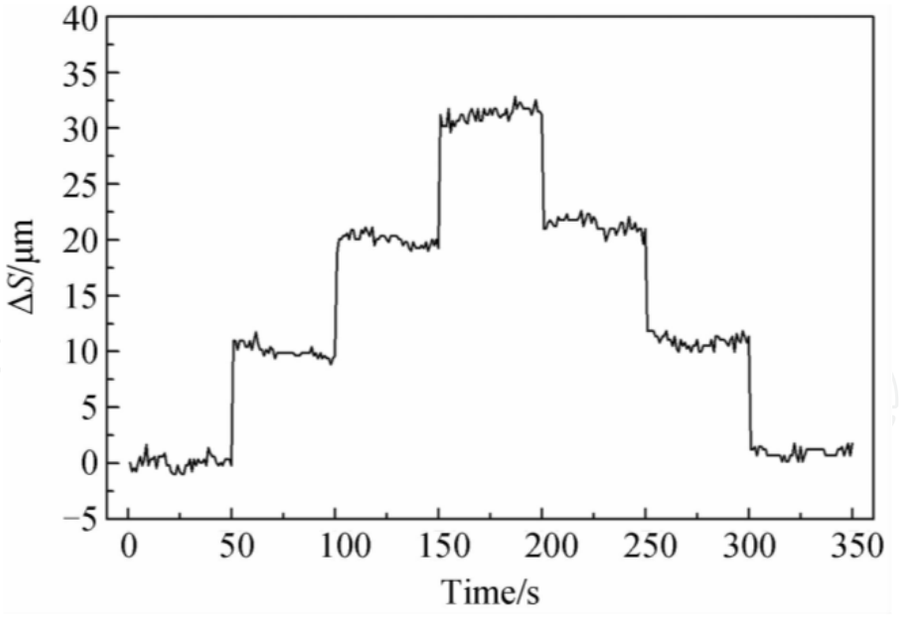

Figure 19. Experiment result using GH shift measurement

3.3. Optical modulators

The configuration of electro-optic (EO) modulator is a SMCW on a glass (K9) flat. The cover and the substrate are both gold film, and the waveguide is EO polymer film. An applied

electric field modulates refractive index of the EO polymer, resulting in the change of the effective refractive index for the guided modes, shifting the resonance dips along the angular direction in ATR spectrum. If we define γ_{33} as the EO coefficient of the polymer and E is the applied electric field across the EO polymer film. The refractive index change of guiding layer Δn_1 is written as [19]:

$$\Delta n_1 = -\frac{1}{2} n_1^3 \gamma_{33} E \tag{39}$$

At the midst of the fall-offs of resonance dip, where a considerably good linearity is observed, the change of the light reflectivity ΔR is:

$$\Delta R = \frac{1}{\sqrt{\varepsilon_3}\cos\theta}\left(\frac{\partial R}{\partial \theta}\right)\left(\frac{\partial N}{\partial n_1}\right)\Delta n_1 = \frac{S_R n_1^4 \gamma_{33}}{\sin 2\theta} E \tag{40}$$

Therefore the reflected light is modulated by the applied electric field. Higher sensitivity is obtained at the midst of the fall-off of the resonance dip excited at smaller resonance angle with thicker guiding layer, so that enhanced modulation is realized by enabling the device to operate with stronger modulation depth and lower driving voltage.

In the experiment, the gold film about 300nm was sputtered onto the surface of the K9 glass flat to serve as substrate and one electrode. A PMMA-based second-order nonlinear optical (NLO) side-chain material containing the disperse red chromophore was synthesized through copolymerization for electro-optic device. The polymer was dissolved in toluene, 25% polymer to 75% toluene by weight. A 12-thick polymer film was spin coated onto the gold film substrate, and then was tempered at 40° in a vacuum for 12 hours to remove the residual solvent. The refractive index of polymer is 1.52 at wavelength 832nm. In order to remove the centrosymmetric structure of the chromophores, the film was corona-poled in the air by an applied electric voltage of 4000V at 110° for 25 min with inter-electrode distance being 20mm, and cooled down to room temperature with the field still applied. Finally, the upper gold film about 30nm thick was deposited on the polymer film by sputtering technique to serve as the coupling layer and another electrode. The complex dielectric constant of the gold film is $\varepsilon_2 = -28 + i1.6$. The EO coefficient γ_{33} of polymer measured at 832 nm using improved ATR method is 11.9 pmV. A collimated TM-polarized beam with 832nm wavelength is used. The modulation working angle was chosen at the midst of the fall-off of the resonance dip excited at resonance angle 9.7°. A sinusoidal electrical field was applied across the two electrodes with 10 $V_{p\text{-}p}$ driving voltage at 1MHz, the electro-optic modulation process was obtained. The oscilloscope traces of modulating voltage and reflected intensity versus time are shown, respectively, in Fig.20. The modulation depth was measured to be 8.7%. However, under the same electrical field the modulation depth was only 5.6% when the resonance dip at 28.9° was used, which is attributed to lower sensitivity at larger resonance angle. The total insertion loss of the sample was 1.08 dB[20].

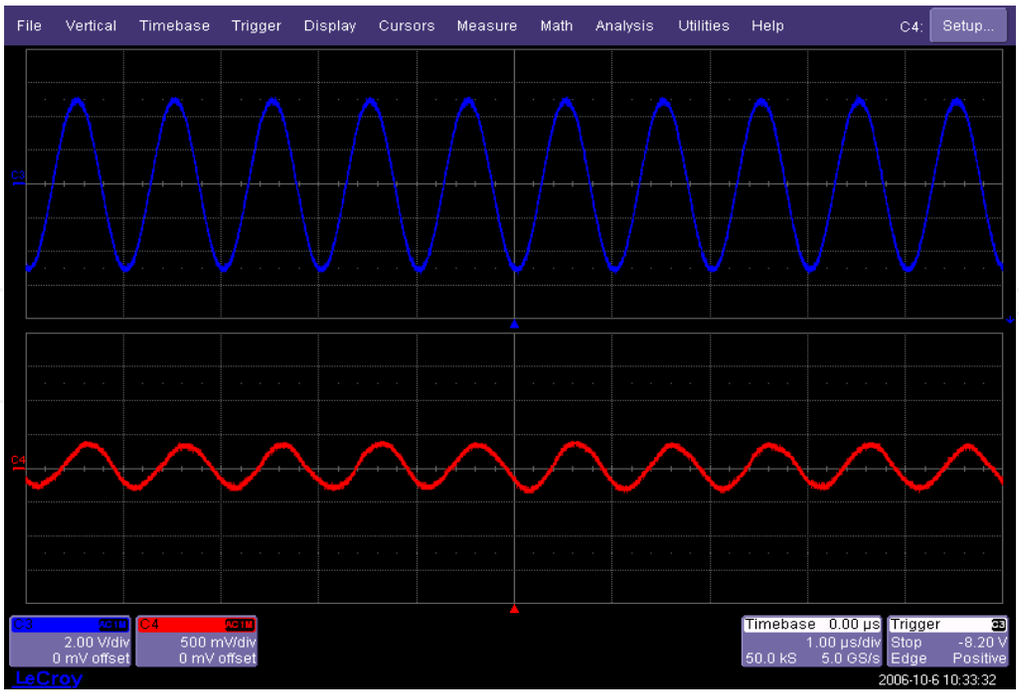

Figure 20. Oscilloscope traces of modulating voltage versus time (upside) and the reflected intensity versus time (downside).

3.4. Slow light devices

The scheme diagram of the SMCW for verifying slow light effect is illustrated in Fig. 21. The advantages of this geometry are that the slow light properties can be tailored to the desired wavelength and the delay is tunable by varying the incident angle and the parameters of the guiding layer. This is important because the applications of slow light require a degree of tunability. These make the proposed slow light scheme useful and practical.

Test experiment has been performed with the waveguide parameters as follows: $\varepsilon_1 = 2.89$, $\varepsilon_2 = -19 + 0.5i$ (silver films), $\varepsilon_3=1.0$, d=2mm (glass slab), h=30 nm, λ=632.8 nm, and θ=3°. An additional silver stripe (about 500nm thick and 1.1 cm wide) is fabricated in the middle of this layer to prevent light leakage. According to Eq.(19), one finds that $\mathrm{Im}(\beta^0)=0.1158526\mathrm{mm}^{-1}$, which shows that the signal power is about 10% after propagating along the guiding layer for about 1 cm. The proposed structure is completely different from the conventional Fabry-Perot cavity, and those similar folded optical delay lines where the incident ray of light bounces in the cavity between the two interfaces (mirrors) before it exits [21]. From Eq. (12), the slow light effect can be observed only when a specific UHM that propagates along the guiding layer is excited, thus the proposed slow light scheme does not rely on obtaining long optical paths. This proposed slow light mechanism can also be interpreted in terms of the anomalous dispersion of the UHMs, which is depicted in Fig.22. It is demonstrated in Fig.22 that anomalous dispersion curves of the proposed structure exhibit an extremely flattened region (slow light region) in the vicinity of zero wave number ($N\rightarrow 0$).

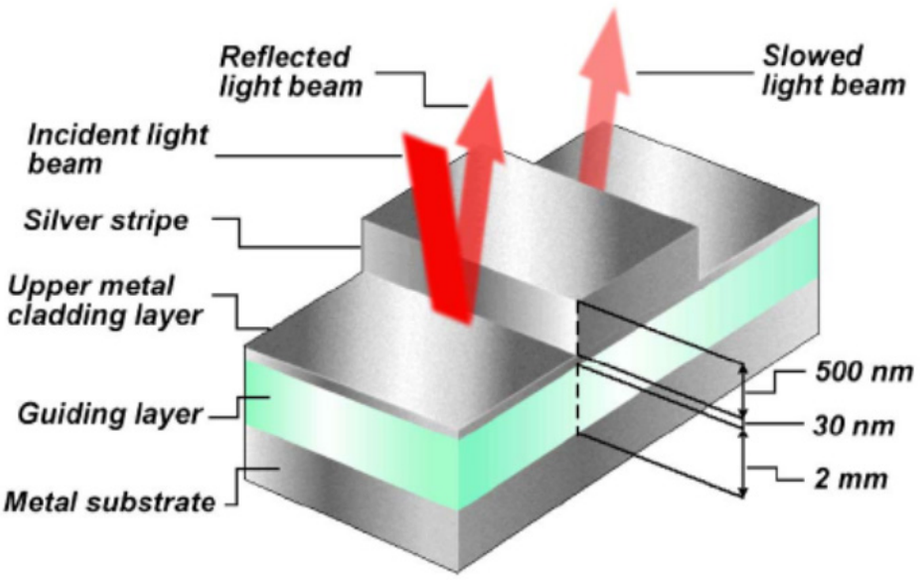

Figure 21. Schematic layout of the SMCW for verifying slow light effect

In the experimental arrangement, the source is a collimated light beam at a wavelength of 650 nm, which is modulated by an EO modulator to produce a signal of 1.0 GHz sinusoidal pulse train. Two photodiodes are setup to detect the light intensity. The first photodiode (PD1) takes in the reflected light beam, which serves as the reference beam. The second photodiode (PD2) is used to measure the time delay of the slowed light beam. The tunable delay is measured by an oscilloscope with the bandwidth of 2 GHz. We measure the delay times Δt at different fixed incident angles, which become larger as the incident angle θ becomes smaller. The experimental results are illustrated in Fig.23. After propagating through a 1.1-cm-long active region, a delay of 2.165 ns was achieved, that corresponds to group velocities less than 0.017c. Further decreasing the incident angle could generate more delay [22].

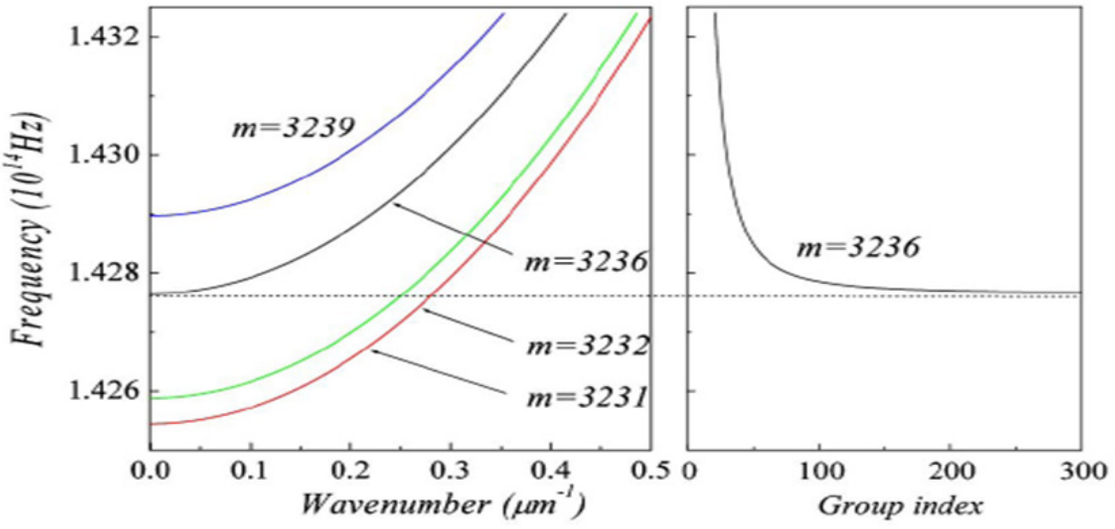

Figure 22. Dispersion curves and group index characteristics of ultrahigh-order modes with parameters ε_2 =–19 + 0.5i , ε_1 = 2.89, and d = 2 mm.

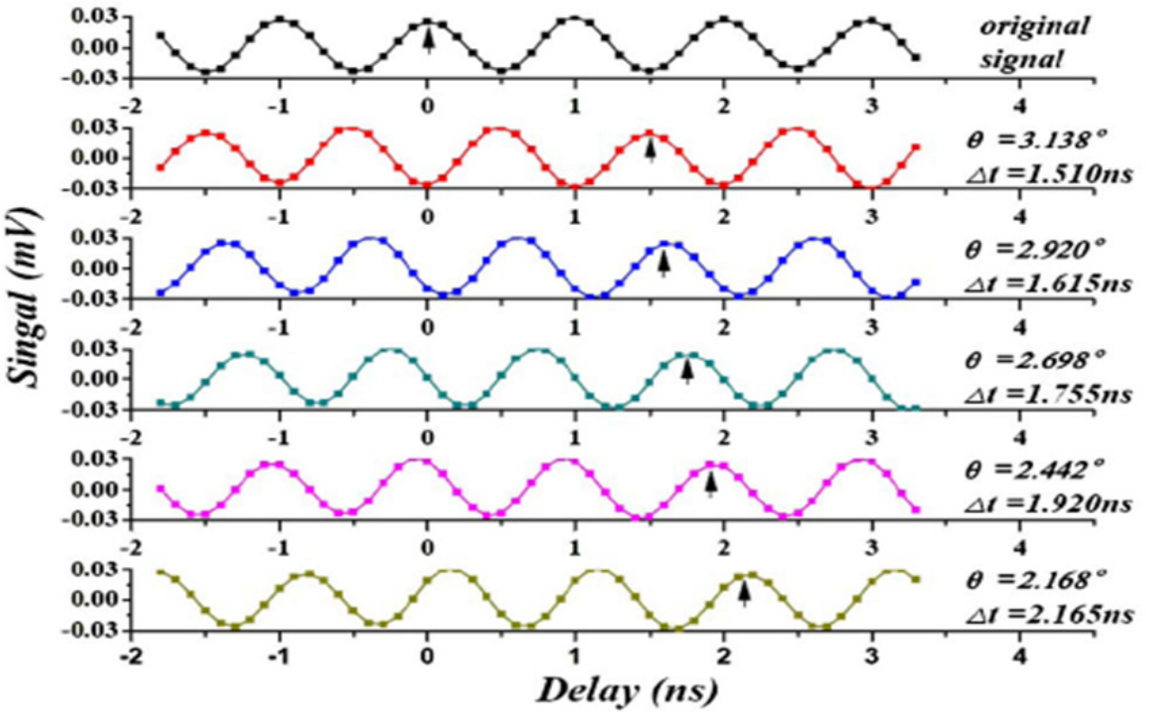

Figure 23. Delay tuning of slow light in an SMCW structure by adjusting the incident angle.

4. Conclusion

The properties of UHM in a SMCW and its applications on optical devices have been demonstrated in this chapter. It is found that the effective refractive index of UHM is sensitive to the refractive index, the thickness of the waveguide layer and the incident wavelength. UHM has also shown strong dispersion and polarization independent effects. Then, a polarization independent and tunable comb filter based on SMCW has been introduced, which has greater than 12 dB channel isolation, less than 0.2 dB insertion loss, and accurate 0.8 nm channel spacing in optical communication range. Taking the reflectivity and GH shift as the sensing probe, a new oscillating wave sensor is investigated to measure minute changes in various parameters such as the refractive index of the guiding layer, the thickness of the waveguide layer and the incident wavelength. It is demonstrated both theoretically and experimentally that its sensitivity is enhanced by one order of magnitude than that of evanescent wave sensor. Furthermore, an EO polymer modulator employing an SMCW is presented. The fabricated modulator achieves an 8.2% modulation depth with $10V_{p\text{-}p}$ driving voltage at 1 MHz. Finally, a new mechanism for slow light assisted by UHMs excited in the SMCW is introduced. A delay bandwidth product greater than 2 is demonstrated in the experiment with a signal of 1.0 GHz sinusoidal pulse train. Without use of any coherent or material resonance, this scheme is not subject to limitations of the delay bandwidth product and can generate arbitrarily small group velocities over an unusually large frequency bandwidth. We think such SMCWs possess unique and advantageous properties over the state-of-the-art and may have great potential for next generation optical devices.

Author details

Lin Chen
Engineering Research Center of Optical Instrument and System, Ministry of Education,
Shanghai Key Lab of Modern Optical System,
University of Shanghai for Science and Technology, China

Acknowledgement

The author thanks Ning Yang and YinQi Bao, students from the University of Shanghai for Science and Technology, for editing the manuscript of this chapter. This work is partly supported by the Leading Academic Discipline Project of Shanghai Municipal Government (S30502), "Chen Guang" Research Fund from Shanghai Municipal Education Commission and Shanghai Education Development Foundation (09CG49), and the Basic Research Program of Shanghai from Shanghai Committee of Science and Technology (11ZR1425000).

5. References

[1] O. Solgaard, F. Ho, J. I. Thackara, and D. M. Bloom, High frequency attenuated total internal reflection light modulator, *Appl. Phys. Lett*., Vol. 61, No. 21, pp. 2500-2502 (1992).

[2] B. Yu, G. Pickrell, and A. Wang, Thermally tunable extrinsic Fabry-Perot filter, *IEEE Photon, Technol. Lett*., Vol. 16, No. 10, pp. 2296-2298 (2004).

[3] R. Horvath, H. C. Pedersen, and N. B. Larsen, Demonstration of reverse symmetry waveguide sensing in aqueous solutions, *Appl. Phys. Lett.*, Vol. 81, No. 12, pp. 2166-2168 (2002).

[4] H. Shin and S. Fan, All-Angle Negative refraction for surface plasmon waves using a metal-dielectric-metal structure, *Phys. Rev. Lett.*, Vol. 96, No. 7, pp. 3907-3910 (2006).

[5] H. F. Lu, Z. Q. Cao, H. G. Li and Q. S. Shen, Study of ultrahigh-order modes in a symmetrical metal-cladding optical waveguide, *Appl. Phys. Lett.*, Vol. 85, No. 20, pp. 4579-4581 (2004).

[6] H. G. Li, Z. Q. Cao, H. F. Lu, and Q. S. Shen, Free-space coupling of a light beam into a symmetrical metal-cladding optical waveguide, *Appl. Phys. Lett.*, Vol. 83, No. 14, pp. 2757-2759 (2003).

[7] X. M. Liu, P. F. Zhu, Z. Q. Cao, Q. S. Shen, and J. L. Chen, Prism coupling of ultrashort light pulses into waveguides, *J. Opt. Soc. Am. B*, Vol. 23, No. 2, pp. 353-357 (2006).

[8] L. Chen, Y. M. Zhu, D. W. Zhang, Z. Q. Cao and S. L. Zhuang, Investigation of the limit of lateral beam shifts on a symmetrical metal-cladding waveguide, *Chin. Phys. B*, Vol. 18, No. 11, pp. 4875-4880 (2009).

[9] X. B. Liu, Z. Q. Cao, P. F. Zhu, Q. S. Shen, and X. M. Liu, Large positive and negative lateral optical beam shift in prism-waveguide coupling system, *Phys. Rev. E*, Vol. 73, No. 5, pp. 6617-6621 (2006).

[10] L. Chen, Z. Q. Cao, F. Ou, H. G. Li, Q. S. Shen, and H. C. Qiao, Observation of large positive and negative lateral shifts of a reflected beam from symmetrical metal-cladding waveguides, *Opt. lett.*, Vol. 32, No.11, pp. 1432-1434 (2007).

[11] H. Lu, Z. Cao, H. Li, Q. Shen, and X. Deng, Polarization-independent and tunable comb filter based on a free-space coupling technique, *Opt. Lett*., Vol. 31, No.3, pp. 386-388 (2006).

[12] J. Villatoro and A. Garcia-Valenzuela, Sensitivity of optical sensors based on laser-excited surface-plasmon waves, *Appl. Opt*., Vol. 38, No. 22, pp. 4837-4844 (1999).

[13] L. Chen, Z. Q. Cao, Q. S Shen, X. X. Deng, F. Ou, and Y. J. Feng, Wavelength sensing with subpicometer resolution using ultrahigh order modes, *J. Lightwave Technol*., Vol. 25, No.2, pp. 539-543 (2007).

[14] J. H. Gu, G. Chen, Z. Q. Cao, and Q. S. Shen, An intensity measurement refractometer based on a symmetric metal-clad waveguide structure, *J. Phys. D: Appl. Phys*., Vol. 41, No.18, pp. 5105 (2008).

[15] J. Homola, S. S. Yee, and G. Gauglitz, Surface plasmon resonance sensors: review, *Sens. Actuators B,* Vol. 54, No. 1-2, pp. 3-15 (1999).

[16] Y. Wang, H. G. Li, Z. Q. Cao, T. Y. Yu, Q. S. Shen, and Y. He, Oscillating wave sensor based on the Goos–Hänchen effect, *Appl. Phys. Lett*., Vol. 92, No. 06, pp. 1117-1119 (2008).

[17] F. Chen, Z. Q. Cao, Q. S. Shen, X. X. Deng, B. M. Duan, W. Yuan, M. H. Sang, and S. Q. Wang, Nanoscale displacement measurement in a variable-air-gap optical waveguide, *App. Phys. Lett*., Vol. 88, No. 16, pp. 1111-1112 (2006).

[18] T. Y. Yu, H. G. Li, Z. Q. Cao, Y. Wang, Q. S. Shen, and Y. He, Oscillating wave displacement sensor using the enhanced Goos–Hänchen effect in a symmetrical metal-cladding optical waveguide, *Opt. Lett*., Vol. 33, No. 9, pp. 1001-1003 (2008).

[19] Y. Jiang, Z. Cao, Q. Shen, X. Dou, Y. Chen, and Y. Ozaki, Improved attenuated total reflection technique for measuring the electro-optic coefficients of nonlinear optical polymers, *J. Opt. Soc. Am. B*, Vol. 17, No. 5, pp. 805-808 (2000).

[20] X. X. Deng, P. P. Xiao, X. Zheng, Z. Q. Cao, Q. S. Shen, K. Zhu, H. G. Li, W. Wei, S. X. Xie, and Z. J. Zhang, An electro-optic polymer modulator based on the free-space coupling technique, *J. Opt. A: Pure Appl. Opt*., Vol. 10, No. 1, pp. 5305 (2008).

[21] D. R. Herriott and H. J. Schulte, Folded optical delay lines, *Appl. Opt*., Vol. 4, No. 8, pp. 883-889 (1965).

[22] W. Yuan, C. Yin, H. G. Li, P. P. Xiao, and Z. Q. Cao, Wideband slow light assisted by ultrahigh-order modes, *J. Opt. Soc. Am. B*, Vol. 28, No. 5, pp. 968-971 (2011).